International Journal of Impact Engineering 214 (2026) 105727

Contents lists available at ScienceDirect

International Journal of Impact Engineering

journal homepage: www.elsevier.com/locate/ijimpeng

Dynamic properties of glued laminated timber beams with finger-joints subjected to impact loading

Gioele Montalbetti [a,*], Alex Sixie Cao [a,b], Andrea Frangi [a]

[a] ETH Zurich, Institute of Structural Engineering, Stefano-Franscini-Platz 5, Zurich, 8093, Switzerland
[b] Empa - Swiss Federal Laboratories for Materials Science and Technology, Structural Engineering Research Laboratory, Ueberlandstrasse 129, Dubendorf, 8600, Switzerland

ARTICLE INFO

Keywords:
Progressive collapse
Impact loading
Glued laminated timber
Strain rate
Dynamic strength increase
Rate dependency

ABSTRACT

As mass timber construction grows in scale and complexity, understanding its response when subjected to highly dynamic loading is essential. While rate-dependent material behaviour is well characterised for steel and reinforced concrete, corresponding material models for timber remain limited. Existing design standards and guidelines typically rely on constant dynamic strength increase or simplified load-duration factors, which may under- or overestimate the ultimate resistance in short duration, high strain rate events. This study conducted 36 full-scale pendulum impact hammer tests on spruce glued laminated timber beams with finger-joints at ETH Zurich, varying beam length and impact velocity to achieve strain rates between 0.50 and 2.00 s^{-1}. The results, combined with data from literature, enabled the calibration of a Cowper–Symonds power law for glued laminated timber. Dynamic strength increase factors ranged from 1.00 to 1.70. Energy-based analyses revealed substantial energy dissipation, with specimens absorbing five to eight times the elastic strain energy in the post-peak phase. These findings provide a robust basis for rate-dependent modelling of timber subjected to impact loading and may inform improved application of dynamic strength increase factors in design standards and guidelines. The quantification of the energy dissipation enables performance-based design of timber subjected to impact loading, supporting controlled member rupture while ensuring full dissipation of the impactor's kinetic energy.

1. Introduction

As the scale and sophistication of mass timber buildings increase, a critical challenge emerges in understanding and ensuring their response when subjected to highly dynamic loading. Highly dynamic loading may occur during progressive collapse [1,2], impact loading [3,4], and similar. During such loading, materials may exhibit higher stiffness, higher ultimate resistance, or both. Due to the extensive use of steel in the automotive and construction industries, its rate-dependent effects are well known and quantified [5–7]. Similarly, for reinforced concrete, a variety of material models have been developed [8–10]. Conversely, suitable rate-dependent material models for timber are still largely absent.

Design standards and guidelines cover dynamic effects through constant prescriptive dynamic strength increase factors k_{dyn} [11,12], defined as the ratio between dynamic and quasi-static resistance, which lead to inconsistency in design and may under- or overestimate the ultimate resistance. The Canadian standard CSA S850:23 [11] and Russian standard SP 64.13330.2017 [12] differentiate between loading-rate and load duration effects. CSA S850:23 defines the dynamic strength S_D as $S_D = SIF \cdot DIF \cdot S_S$ for blast loading, where SIF represents the strength increase factor used to transform design-level resistances to mean values, and $DIF = k_{dyn}$ denotes the dynamic strength increase factor used to transform the static strength S_S to the dynamic strength S_D. In addition to the dynamic strength increase factor, a load duration factor K_D of 1.15 is prescribed when considering the blast resistance of timber components. The dynamic increase factor DIF for glued laminated timber in flexure is limited to 1.1. Similarly, SP 64.13330.2017 [12] offers a strength increase value for coniferous woods, prescribing a general strength increase of 1.1 at the design level for impulse and shock loading with peak load durations between 10^{-8} and 10^{-1} s. In contrast, ASCE/SEI 59-11 [13] acknowledges the significance of dynamic material strength under blast loading but assumes no strength increase for timber. Neither the current Eurocode EN 1995-1-1:2024 [14] nor the Swiss standard SIA 265:2021 [15] explicitly incorporates a dynamic strength increase factor based on the loading rate. Instead, dynamic effects are addressed indirectly through a load

* Corresponding author.
E-mail address: gmontalbe@ethz.ch (G. Montalbetti).

https://doi.org/10.1016/j.ijimpeng.2026.105727
Received 28 November 2025; Received in revised form 8 March 2026; Accepted 16 March 2026
Available online 18 March 2026
0734-743X/© 2026 The Authors. Published by Elsevier Ltd. This is an open access article under the CC BY license (http://creativecommons.org/licenses/by/4.0/).

duration factor k_{mod}, expressed as $X_d = k_{mod} X_k / \gamma_m$, where X_k is the characteristic value, γ_m the partial factor, and X_d the design value of the material property. These provisions reduce the dynamic response to a simplified time-based adjustment, with $k_{mod} = 1.1$ in EN 1995-1-1:2024 and the equivalent of k_{mod} for the Swiss standard SIA 265:2021 $\eta_t = 1.4$. However, the load duration factor k_{mod} was primarily developed for assessing creep and not impact loading phenomena [16–18].

Past research on the rate-dependent behaviour of glued laminated timber has focused on simulated blast loading [19], drop-weight four-point bending tests with [20] and without [21] temperature effects, and the quantification of energy-related quantities for spruce glued laminated timber without finger-joints [22]. Lacroix and Doudak [19] investigated the influence of different finger-joint arrangements and their implications for the dynamic stiffness and ultimate resistance increase. The study reported a strength increase factor k_{dyn} of 1.14 for strain rates $\dot{\varepsilon}$ between 0.14 and 0.51 s^{-1}. For glued laminated timber with continuous finger-joints, no dynamic stiffness increase was measured. The tests were conducted on 20f-E and 24f-ES strength grade glued laminated timber beams. No production standard or timber species was disclosed. Wight et al. [21] employed a drop-weight four-point bending test setup, reporting a slightly lower k_{dyn} of 1.13 for strain rates ranging from 0.57 to 1.05 s^{-1}. In a subsequent study, Wight et al. [20] performed additional tests at room and sub-zero temperatures, reporting higher k_{dyn} values of up to 1.31 for strain rates ranging from 1.13 to 1.38 s^{-1}, with no statistically significant influence of sub-zero temperature effects. Both studies [20,21] performed tests on NordicLam+ 24f-ES grade spruce-pine-fir glued laminated timber beams produced in accordance to CSA O177-23 [23] with strength requirements according to CSA O122-16 [24].

Cao et al. [22] conducted tests on spruce glued laminated timber beams without finger-joints to quantify their energy dissipation potential in the context of low-velocity impact loading. The specimens were strength graded based on the measured moisture adjusted modulus of elasticity and produced according to EN 14080:2013 [25]. By idealising an extension of the load–displacement curve, Cao et al. [22] derived energy-based $k_{dyn,E}$ ratios, defined as the ratio between the total dissipated energy and the strain energy accumulated up to the quasi-static resistance. The idealised energy-based $k_{dyn,E}$ for glued laminated timber without finger-joints ranged between 4.3 and 5.7 for strain rates $\dot{\varepsilon}$ between 0.64 and 0.70 s^{-1}.

Early research on the development of models for the dynamic loading of timber was conducted by Wood [16], where an empirical model to describe load duration effects was developed. The aforementioned empirical model used a hyperbolic relationship to describe the load duration effects and was calibrated using experimental data from impulsive loading to creep. Instead of focusing on load duration effects, Lacroix and Doudak [26] introduced rate-dependent effects using a logarithmic function that was calibrated with data from simulated and live blast experiments. Subsequently, Wight et al. [20] used a similar functional form based on the natural logarithm. Another widely used model for describing rate-dependent effects is the empirical overstress power law by Cowper and Symonds [27]. Originally, the overstress power law was used to describe the evolution of the yield stress of cantilever steel beams subjected to impact loading [27]. Since then, it has been widely applied to various metallic materials [28–31] but has also found application in other materials. For instance, it was used to extend a hyper-viscoelastic constitutive model for polyurethane [32], calibrate a regression model for linear-elastic and perfectly brittle Kevlar fibres [33], derive a scaling law for the dynamic strength of brittle ceramics [34], and to perform finite-element analyses of homogeneous poly(methyl methacrylate) with a uniaxial response in compression and tension similar to that of timber [35]. Furthermore, the same law has been employed to develop a regression model for functionally graded lattice structures reinforced with short carbon fibres [36], and to characterise a wood-based material under uniaxial tension at high strain rates [37].

In this paper a displacement-based analytical model is developed to determine the ultimate resistance at failure enabling the contribution of additional data to the existing literature [19–21] on the dynamic strength increase k_{dyn} of glued laminated timber with finger-joints. The displacement-based analytical model captures inertial effects and is extended to quantify the accumulated strain energy. A novel load–displacement idealisation is introduced to quantify the post-peak dissipated energy through an idealised softening ratio deviating from the idealisation proposed by Cao et al. [22] and leading to a more mechanically consistent representation of the release energy E_r. A regression formula based on the empirical Cowper–Symonds overstress power law is calibrated by combining the results of this study with data from existing literature [19–21]. Based on the developed ultimate resistance regression an additional regression is proposed to quantify the idealised softening ratio. This enables coupling of the dynamic resistance with the total dissipated energy. Overall, this paper aims to advance the understanding of dynamically loaded glued laminated timber with finger-joints by providing a consistent description of the dynamic strength increase k_{dyn} for the ultimate resistance, an idealised model for energy dissipation quantification, and rate-dependent behaviour suitable for structural analysis.

2. Theoretical basis

The theoretical basis is presented and derived for homogeneous linear elastic material behaviour. Common assumptions for the analysis of timber include homogeneous cross-section behaviour with symmetric stress distribution in bending, linear elastic behaviour, and a linear idealisation of the staircase-type post-peak strength reduction [38–40]. A pre-peak delamination of the lamellas leading to a non-homogeneous cross-sectional behaviour could occur for high strength grades but is not expected [22] and was not observed in this study. The linear idealisation of the post-peak response captures the dissipated energy and should not be interpreted as a true load–displacement relation. The strain rate is defined as the strain rate of the outermost fibre in the cross-section [19–21,41] thereby lumping the true distributed micro-level strain rate behaviour into a single value and representing an average of possible asymmetric behaviour in tension and compression.

2.1. Energy balance

At the initial and final positions of a compound or physical pendulum, the angular acceleration $\ddot{\theta}$ and angular velocity $\dot{\theta}$ are equal to zero, therefore the system can be described by its potential energy $m_p g h$. By applying trigonometric relations, the difference in potential energy between the initial and final position ΔE can be expressed as [22]:

$$\Delta E = m_p g L_{CM} (\cos\theta_1 - \cos\theta_0), \tag{1}$$

where m_p is the mass of the pendulum, L_{CM} is the location of the centre of mass, θ_0 is the angle of the initial position, θ_1 is the angle at the final position after impact, and $g = 9.81$ m/s^2 is the gravitational acceleration. In an experiment, multiple forms of energy loss should be considered. These include the energy dissipated by the release mechanism of the pendulum E_{c1}, losses due to friction and air resistance E_{c2}, the kinetic energy transferred to the beam K_b, and the energy required for complete rupture of the specimen E_r, commonly referred to as the release energy [22]. The complete energy balance can be expressed as:

$$m_p g h_0 = m_p g h_1 + E_r + E_c + K_b, \tag{2}$$

where $h_0 = L_{CM}\cos\theta_0$, $h_1 = L_{CM}\cos\theta_1$ and $E_c = E_{c1} + E_{c2}$. Solving Eq. (2) for the release energy E_r results in:

$$E_r = m_p g L_{CM} (\cos\theta_1 - \cos\theta_0) - E_c - K_b. \tag{3}$$

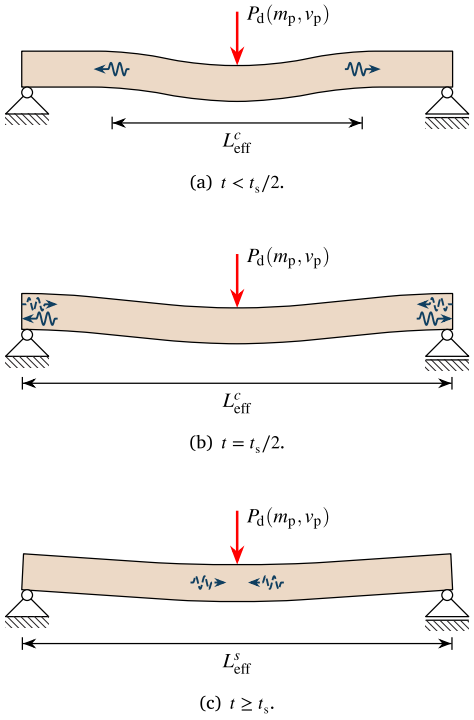


Fig. 1. Impact process of an elastic beam. (a) Transient dynamic phase, where the inertial field is partially activated with an effective length L^c_{eff} and follows the deflected shape of an equivalent clamped system. The shear waves have not fully propagated to the supports yet. (b) Shear waves reach the support and are reflected on the free surface. The inertial field still follows the deflected shape of an equivalent clamped system but with an equivalent length $L^c_{eff} = L$. (c) Fully activated inertial field following the deflected shape of a simply supported beam.

2.2. Wave propagation and impact process

During an impact process, loads propagate with different velocities through the specimen. In an elastic isotropic medium, longitudinal waves propagate with a velocity c_l of:

$$c_l = \sqrt{\frac{E}{\rho}}, \tag{4}$$

where E is the modulus of elasticity and ρ the density. Shear waves propagate with a velocity c_s of:

$$c_s = \sqrt{\frac{G}{\rho}}, \tag{5}$$

where G is the shear modulus. Because bending waves propagate with varying frequency during an impact process [42], the wave propagation is dispersive [43]. Dispersive waves propagate with a group velocity. For rectangular cross-sections the bending wave group velocity c_{gb} is defined as:

$$c_{gb} = 2\left(\frac{Eh^2}{12\rho}\right)^{1/4}\sqrt{\omega_n}, \tag{6}$$

where h is the height of the cross-section and ω_n is one of the natural frequencies of the beam. To approximate the deflections w of a simply supported beam subjected to a point load at mid-span, the first eigenfrequency ω_1 is selected. A fully activated inertial field, as shown in Fig. 2(a), is only valid after the transverse shear waves have travelled to the supports and back to the load application point. The full process is illustrated in Fig. 1.

2.3. Load model

During an impact process, the projectile undergoes deceleration while the specimen is simultaneously accelerated, generating an inertial force field distributed along the beam [44]. This dynamic equilibrium is illustrated in Fig. 2(a). This study relies on displacement measurements to determine the ultimate resistance. To express different quantities of the dynamic equilibrium of an elastic beam with a displacement measurement w at the mid-span, the displacement w is expressed for the entirety of the loading, P_d, q_{in}, and time t. Therefore, $w = f(P_d, q_{in}, t)$. The resulting mid-span displacement w due to a concentrated load P_d and a distributed inertial load q_{in}, incorporating both bending and shear effects, is given by:

$$w = w^P_b + w^P_v + w^{in}_b + w^{in}_v = \frac{P_d L^3}{48EI} + \frac{P_d L}{4\kappa GA} + \frac{17 q_0 L^4}{1680EI} + \frac{q_0 L^2}{10\kappa GA}, \tag{7}$$

where L is the span length, I the second moment of area, A the cross-sectional area of the specimen, $q_0 = -P_d \rho A/m_p$ the maximum inertial load amplitude at mid-span, and $\kappa = 5/6$ the shear area correction factor for rectangular cross-sections. The derivation is provided in Appendix A.

2.4. Displacement-based approach

From Eq. (7), the spring stiffness $k_{b,v}$ at the mid-span due to a point load P_d and inertial loading q_{in}, accounting for both bending and shear deformations, can be derived. The result is:

$$k^{P,in}_{b,v} = \frac{48EI}{L^3}\left(1 + 12\alpha\frac{1}{L^2} - \frac{17}{35}\beta - \frac{24}{5}\alpha\beta\frac{1}{L^2}\right)^{-1} \tag{8}$$

with

$$\alpha \equiv \frac{EI}{\kappa GA} \quad \text{and} \quad \beta \equiv \frac{m_b}{m_p},$$

where m_b is the mass of the beam. If the inertial force field is neglected:

$$k^P_{b,v} = \frac{48EI}{L^3}\left(1 + 12\alpha\frac{1}{L^2}\right)^{-1}, \tag{9}$$

and if the shear contribution is neglected:

$$k^P_b = \frac{48EI}{L^3}. \tag{10}$$

By having determined the stiffness of the beam at mid-span k, the dynamic force at failure $P_{d,R}$ can be determined from $P_{d,R} = k\delta_{el}$.

2.5. Dynamic strength increase factor

The acting dynamic bending moment M_d is a superposition of the bending moment from the point load P_d and the inertial loading q_{in}:

$$M_d = M^P_d + M^{in}_d = \frac{P_d L}{4} - \frac{P_d \rho A L^2}{10 m_p}. \tag{11}$$

By taking the ratio of the acting dynamic bending stress $f_{m,d} = M_d/W$ to the mean quasi-static bending resistance $f_{m,s}$ the dynamic strength increase factor k_{dyn} is defined as:

$$k_{dyn} = \frac{f_{m,d}}{f_{m,s}}. \tag{12}$$

2.6. Strain energy approach

As described by Cao and Frangi [41] the energy release E_r of an elastic beam loaded with a concentrated load at mid-span with a linear softening branch can be expressed through an equivalent impact force $P_{d,E}$ by integrating the elastic strain energy $U = U_M + U_V$ with shear deformations. The expression for a simply supported elastic beam loaded at mid-span is:

$$E_r = U_M + U_V = \frac{P^2_{d,E} L^3}{96EI} + \frac{P^2_{d,E} L}{8\kappa GA}. \tag{13}$$

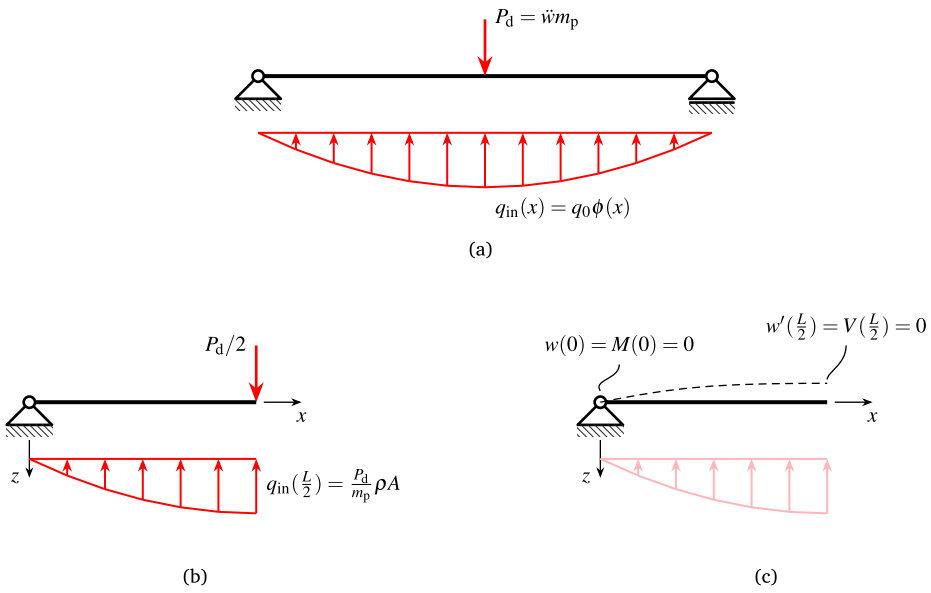


Fig. 2. Assumed system and loading for dynamic equilibrium. (a) Simply supported beam with concentrated impact force P_d and distributed inertial load $q_{in}(x)$. (b) Half-space representation of loading of the beam. (c) Boundary conditions and deflection shape of the beam subjected solely to the inertial load $q_{in}(x)$.

To account for the inertial loading depicted in Fig. 2, analytical expressions of the bending moments $M(x)$ and shear forces $V(x)$ must be developed based on the specific loading scenario. By integrating the bending moment $M(x)$ and shear force $V(x)$ over the beam length L, the following expression for the combined strain energy is obtained:

$$U_M = \frac{1}{EI}\int_0^{L/2} M^2(x)\mathrm{d}x = \frac{P_{d,E}^2}{EI}\int_0^{L/2}\left(\frac{1}{2}x - \frac{\rho A}{m_p}\left(-\frac{1}{2}\frac{x^3}{L} + \frac{1}{5}\frac{x^5}{L^3} + \frac{5L}{16}x\right)\right)^2 \mathrm{d}x, \tag{14}$$

$$U_V = \frac{1}{\kappa GA}\int_0^{L/2} V^2(x)\mathrm{d}x = \frac{P_{d,E}^2}{\kappa GA}\int_0^{L/2}\left(\frac{1}{2} - \frac{\rho A}{m_p}\left(-\frac{3}{2}\frac{x^2}{L} + \frac{x^4}{L^3} + \frac{5L}{16}\right)\right)^2 \mathrm{d}x. \tag{15}$$

By factoring out the idealised energy-equivalent impact force $P_{d,E}$, the release energy E_r can be expressed as:

$$P_{d,E} = \sqrt{\frac{E_r}{\lambda + \mu}}, \tag{16}$$

where

$$\lambda \equiv \frac{1}{EI}\int_0^{L/2}\left(\frac{1}{2}x - \frac{\rho A}{m_p}\left(-\frac{1}{2}\frac{x^3}{L} + \frac{1}{5}\frac{x^5}{L^3} + \frac{5L}{16}x\right)\right)^2 \mathrm{d}x \quad \text{and}$$

$$\mu \equiv \frac{1}{\kappa GA}\int_0^{L/2}\left(\frac{1}{2} - \frac{\rho A}{m_p}\left(-\frac{3}{2}\frac{x^2}{L} + \frac{x^4}{L^3} + \frac{5L}{16}\right)\right)^2 \mathrm{d}x.$$

However, for a simply supported elastic beam subjected to a point load at mid-span, the closed-form solution reduces to [22]:

$$P_{d,E} = \sqrt{\frac{E_r}{\frac{L^3}{96EI} + \frac{L}{8\kappa GA}}}. \tag{17}$$

As shown in Fig. 3, the strain energy approach by Cao et al. [22] assumes an extension of the maximum resistance $P_{d,R}$ to express the release energy E_r with an analogous strain energy represented by the area enclosed by an energy-equivalent force $P_{d,E}$. By knowing the displacement at failure δ_{el} and the stiffness k of the specimen at the load-introduction, the maximum resistance $P_{d,R}$ can be determined. The

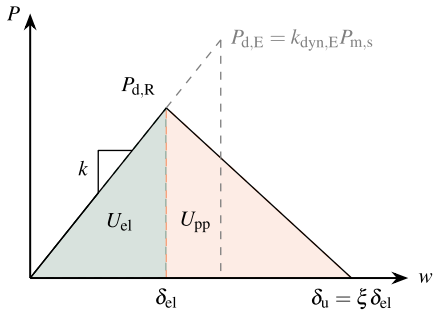


Fig. 3. Schematic of the strain energy approach proposed by Cao et al. [22] defined by an energy-equivalent force $P_{d,E}$ derived from the maximum resistance $P_{d,R}$ shown in grey, and the proposed linear softening idealisation with ultimate displacement δ_u. The total release energy E_r includes the elastic strain energy U_{el} and the post-peak contribution U_{pp}.

release energy of the specimen is the sum of the elastic strain energy U_{el} and post-peak energy U_{pp}. Assuming a triangular load–displacement curve with a linear softening branch, the ultimate displacement δ_u can be expressed by a softening ratio ξ multiplied by the displacement at failure δ_{el}. This provides a more mechanically consistent representation of the release energy E_r.

To express the energy-equivalent force $P_{d,E}$, Cao et al. [22] introduced an energy-equivalent dynamic increase factor:

$$k_{dyn,E} = \frac{P_{d,E}}{P_{m,s}}, \tag{18}$$

where $P_{m,s}$ is the equivalent force of the mean quasi-static bending moment resistance. The energy-equivalent dynamic increase factor can also be expressed through the dynamic strength increase factor k_{dyn} and softening ratio ξ:

$$k_{dyn,E} = \sqrt{k_{dyn}^2 \xi}. \tag{19}$$

with

$$\xi = \frac{2E_r}{P_{d,R}\delta_{el}}. \tag{20}$$

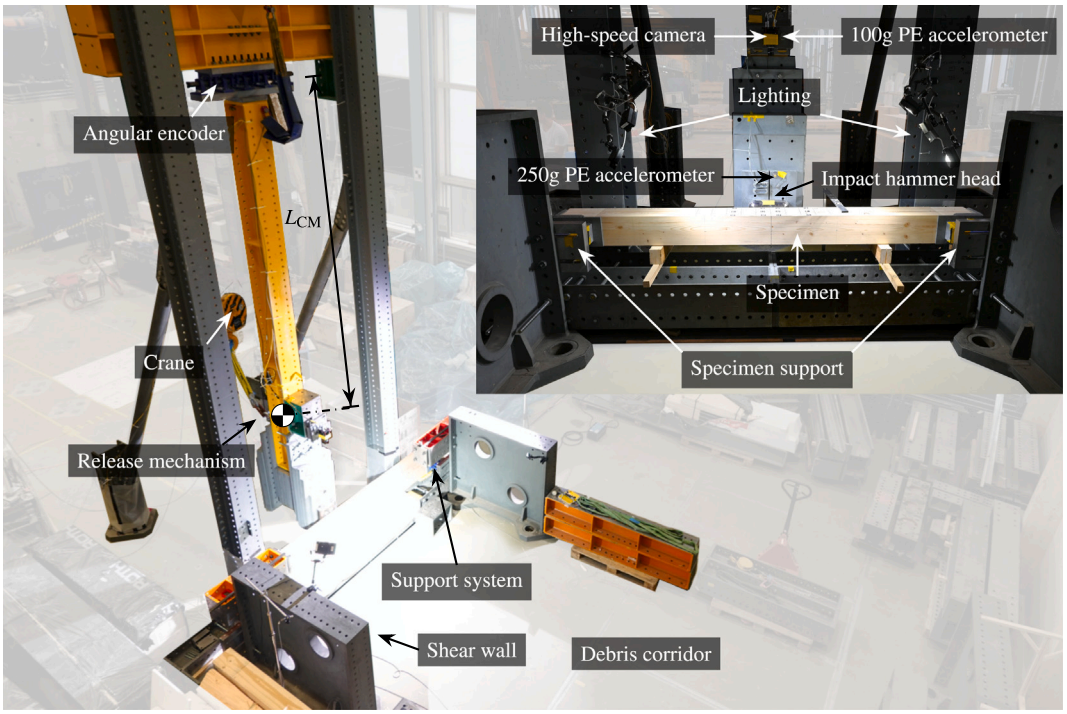


Fig. 4. Experimental pendulum impact hammer setup adapted from Cao et al. [22]. Shown are the pendulum with a total mass of 3475 kg and a centre of mass at L_{CM} = 4700 mm from the hinge, the steel hammer head, and the support frame. The rotational hinge has an angular encoder, two piezoelectric (PE) accelerometers are mounted at the hammer head with a capacity of 250 g and near the high-speed camera with a capacity of 100 g. The high-speed camera is mounted near the centre of mass of the pendulum.

2.7. Strain rate

Definitions of strain rates $\dot{\varepsilon}$ in timber are not consistent. When measuring with strain gauges, the strain rate $\dot{\varepsilon}$ on the tension and compression side can be directly measured [19,21]. However, deriving a representative strain rate $\dot{\varepsilon}$ in bending is challenging as timber can exhibit asymmetric behaviour in compression and tension following its anisotropy. In this study, the strain rate $\dot{\varepsilon}$ is defined through:

$$\dot{\sigma} = \dot{\varepsilon} E = \frac{\dot{M}_{\mathrm{d}}}{W} \quad \therefore \quad \dot{\varepsilon} = \frac{\dot{M}_{\mathrm{d}}}{EW}, \tag{21}$$

where $\dot{\sigma}$ is the stress rate, $\dot{\varepsilon}$ the strain rate, $\dot{M}_{\mathrm{d}}$ the change in bending moment, and W the section modulus. For a simply supported beam with a rectangular cross-section subjected to a point load at mid-span Eq. (21) is reduced to:

$$\dot{\varepsilon} = \frac{6h}{L^2}\dot{w}, \tag{22}$$

where $\dot{w}$ is the velocity of the measured displacement w. The same definition was used by Cao and Frangi [41].

2.8. Constitutive relation

Herein, the material properties of timber are approximated as linear-elastic quasi-brittle with a linear softening branch [45], where the rate-dependent effects are described using an empirical regression for the dynamic strength increase factor. A logarithmic, quadratic polynomial, and a Cowper–Symonds power law were initially considered. The quadratic polynomial and Cowper–Symonds regressions yielded comparable results. Due to the simplicity and widespread use in modelling rate-dependent effects of materials with similar linear-elastic quasi-brittle behaviour as the relevant failure mode in timber [32–37], the Cowper–Symonds overstress power law was selected. It can be defined as:

$$f_{\mathrm{m,d}} = f_{\mathrm{m,s}} k_{\mathrm{dyn}} = f_{\mathrm{m,s}} \left(1 + \left(\frac{\dot{\varepsilon}}{c}\right)^{1/q}\right), \tag{23}$$

where c is the reference strain rate coefficient, also referred to as the reference strain rate $\dot{\varepsilon}_0$, and $1/q$ is the strain rate exponent. The application of the Cowper–Symonds power law in this paper is consistent with its original use and intent by Cowper and Symonds [27] to describe the rate-dependency of the yield stress of cantilever steel beams subjected to impact loading.

2.9. Kinetic energy of the beam

Based on the principle of conservation of momentum, the pendulum transfers a fraction of its kinetic energy to the beam. By applying the modal approximation technique [46], Cao et al. [22] derived the following expression of the kinetic energy of the post-failure beam K_{b}:

$$K_{\mathrm{b}} = \frac{1}{6} m_{\mathrm{b}} v_{\mathrm{p},0}^2 \left(\frac{1}{1 + \frac{1}{3}\frac{m_{\mathrm{b}} L}{m_{\mathrm{p}}}}\right)^2, \tag{24}$$

where $v_{\mathrm{p},0}$ is the pre-impact velocity of the pendulum. As stated in Eq. (3), this energy is subtracted from the global energy balance.

3. Materials and methods

3.1. Pendulum impact hammer setup

The experimental campaign was carried out at ETH Zurich using a custom-built pendulum impact hammer developed by Cao et al. [47]. The overall length of the pendulum, measured from the rotational hinge or pin to the bottom of the hammer head, was 5410 mm. The centre of mass was located at L_{CM} = 4700 mm from the hinge, as shown in Fig. 4. The hammer head, manufactured from S355 steel, had rounded edges and a flat contact surface spanning the full height of the specimen, with a width of 200 mm. The total mass of the impact hammer was 3475 kg, primarily composed of post-tensioned steel plates. Additional mass

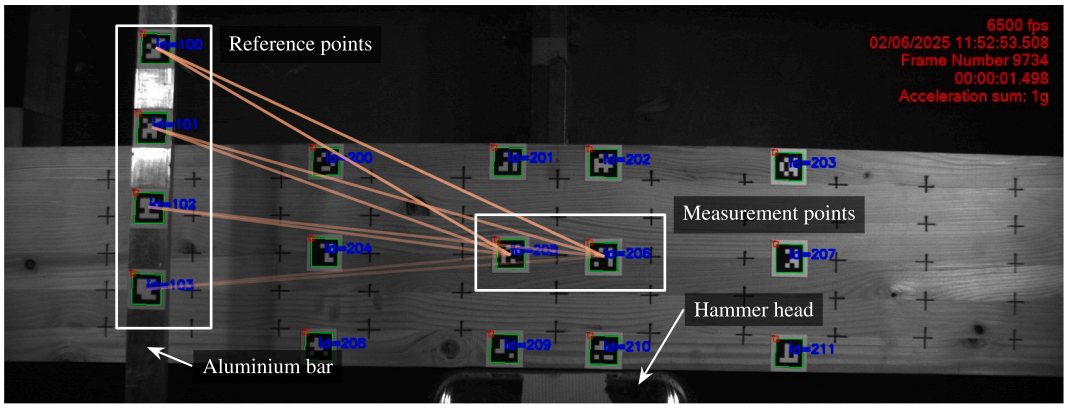


Fig. 5. Displacement measurement setup with ArUco markers and conceptual representation of the measurement datasets. Markers were based on the ArUco 4 × 4 ID 1000 dictionary with dimensions 30 × 30 mm on 40 × 40 mm stickers, occupying approximately 33 × 33 pixels in the high-speed camera images. Displacements were recorded along the mid-span central axis by measuring two points on the specimen against four reference points on a fixed aluminium bar. The datasets were post-processed with a Kalman filter and averaged to reduce noise.

contributions came from the steel hammer head and the pendulum arm. The maximum release angle θ was limited to 85°. To achieve different impact velocities the pendulum was released from 85°, 65°, and 45°. This corresponds to a theoretical potential energy between 159 and 113 kJ. The pendulum was raised to the desired release angle θ_0 using a crane and a remote-controlled electromechanical release mechanism was used to release the pendulum.

A shock-resistant AOS M-VIT 4000 high-speed camera, operating at 6500 frames per second, was mounted above the hammer head on the pendulum. To reduce vibration transmission, the camera was installed on a rubber damping mat. Illumination was provided by six GSVitec Multiled QT lamps, delivering a combined light output of 72 000 lm. Additional video documentation was captured using a GoPro Hero 10 (120 fps) pointed at the supports or at the debris corridor. For digital image tracking, fiducial markers [48] were mounted to the specimens. Reference points were established using an aluminium bar mounted on a stand on the far side of the pendulum. A detailed description of the image tracking procedure is provided in Section 3.3.

To capture the motion of the pendulum, the angular position θ was recorded using a Baumer EIL580P encoder mounted at the axis of rotation. Two piezoelectric accelerometers were installed to capture the impact dynamics, a Kistler 877B250 (250 g) sensor mounted at the hammer head and a lower-capacity Kistler 877B100 (100 g) sensor mounted near the high-speed camera. All sensors were synchronised and sampled at a frequency of 38.4 kHz. The positions of the encoder and accelerometers are illustrated in Fig. 4. Further comprehensive descriptions of the setup are available in the experimental report of Cao et al. [47].

3.2. Intrinsic energy losses

To quantify the dissipated energy due to the release mechanism and air resistance, three free swings at three angles 85°, 65°, and 45° were conducted. A second order polynomial was fitted to the energy losses. This was chosen over an exponential decay as the main dissipative mechanism is aerodynamic drag, which is proportional to the square of the velocity in turbulent flows, and not structural damping of the pendulum impact hammer. To validate this assumption, the energy balance was compared to the observed velocity, as shown in Fig. 8. The specimens which showed poor agreement with the energy balance, were not used for any energy related calculations.

3.3. Displacement tracking

To enable displacement tracking, fiducial markers based on the ArUco [48] dictionary 4 × 4 ID 1000 were used. Each marker measured 30 × 30 mm and was printed on a 40 × 40 mm sticker to ensure a high-contrast boundary region between the black marker and the specimen surface. Image tracking was carried out using the OpenCV library [49] in Python 3.12. Given the resolution of the high-speed camera, each 30 × 30 mm marker occupied approximately 33 × 33 pixels in the image. Prior to testing, the high-speed camera was calibrated using a ChArUco chequerboard pattern to correct for lens distortion and positional parameters. A mean re-projection error of 0.126 pixels was achieved.

As shown in Fig. 5, measurement uncertainty was reduced by measuring the markers of interest against four fixed markers on an aluminium bar. Markers positioned at the hammer head and on the tension side of the beams proved unsuitable for accurate tracking because of severe marker distortions and tearing from local deformations. Instead, the markers located along the central axis at mid-span of the beam were selected. These positions experienced minimal distortion and offered representative displacement measurements. A total of eight independent displacements were measured and post-processed with a Kalman filter prior to being averaged. These were four reference points to two measurement points. The Kalman filter ensured the reduction of measurement noise and removal of artificial peaks based on a Newtonian equation of motion. Averaging the filtered measurements reduced the overall error resulting from the image tracking.

3.4. Material properties

Glued laminated timber beams were supplied by Roth Burgdorf AG and manufactured according to EN 14080:2013 [25] using machine-graded spruce (Picea abies (L.) H. Karst.) boards with a narrow grading band from T14 up to T16 lamellae to minimise material scatter and ensure compliance with a GL24h classification according to EN 14080:2013 [25]. Three specimens with dimensions 200 × 320 × 4800 mm were tested quasi-statically and used as reference values. Volume effects were accounted for in accordance with EN 1995-1-1:2024 [14]. The static modulus of elasticity E_s was determined following the four-point bending test global elastic modulus procedure specified in EN 408:2010 [50]. To determine the shear modulus G, the empirical relation $G = E/16$, specified in the JCSS model code for timber [51] was used. Each specimen's density ρ was calculated based on its measured mass and dimensions. The moisture content was measured at three different locations with a BES Boltzmann Combo 2000 resistance moisture meter. Measurements were taken perpendicular to the grain at a depth of 20 mm. Prior to impact testing, the moisture content was updated and the density and modulus of elasticity E was adjusted in accordance with EN 384:2016 [52].

Table 1
Test program and specimen dimensions. A total of 36 specimens were tested, 35 completely successfully. One specimen missed image tracking due to a faulty trigger of the high-speed camera.

Specimen ID	b (mm)	h (mm)	L (mm)	Material grade	Quantity	Release angle θ_0	Batch
GL24h-200×320×2800-SR1	200	320	2800	GL24h	3[c]	85°	2
GL24h-200×280×2800-SR1	200	280	2800	GL24h	3[c]	85°	2
GL24h-200×240×2800-SR1	200	240	2800	GL24h	3	85°	2
GL24h-200×320×3800-SR2	200	320	3800	GL24h	3[a]	65°	2
GL24h-200×280×3800-SR2	200	280	3800	GL24h	3	65°	2
GL24h-200×240×3800-SR2	200	240	3800	GL24h	3	65°	2
GL24h-200×320×4800-SR3	200	320	4800	GL24h	3	45°	2
GL24h-200×280×4800-SR3	200	280	4800	GL24h	3	45°	2
GL24h-200×240×4800-SR3	200	240	4800	GL24h	3	45°	2
GL24h-160×160×3800-SRX	160	160	3800	GL24h	3[b]	85°	1
GL24h-160×200×3800-SRX	160	200	3800	GL24h	3[b]	85°	1
GL24h-200×320×4800-SRX	200	320	4800	GL24h	3	85°	1
GL24h-200×320×4800-QS	200	320	4800	GL24h	3	–	1

[a] Partially used for energy balance.
[b] Faulty release, partially used for energy balance.
[c] Not used for energy balance.

3.5. Test program and specimens

Rate-dependent effects often only become apparent when strain rates $\dot{\epsilon}$ are treated on a logarithmic scale. To generate sufficiently distinct strain rates $\dot{\epsilon}$ across different specimen configurations, a preliminary study showed that the two most influential variables were the length L of the specimen and the release angle θ_0 of the pendulum. Given the inverse squared relationship of the strain rate $\dot{\epsilon} \propto 1/L^2$ in Eq. (22), the length L of the specimens was varied in three steps, from the minimum to the maximum length that could be easily accommodated by the setup. The second variable was found to be the release angle θ_0. Therefore the release angle θ_0 was modified simultaneously with the length L. Estimates based on the experiments by Cao et al. [22] indicated preliminary strain rates $0.50 \lessapprox \dot{\epsilon} \lessapprox 2.00\ \mathrm{s}^{-1}$.

In addition to the described systematic change of strain rates $\dot{\epsilon}$, a separate batch was incorporated into the experimental campaign. These specimens were tested with the largest possible release angle θ_0 to expand the dataset to different cross-sectional dimensions. This introduces less systematic testing configurations to exclude possible biases emerging from the chosen test program, as two variables are varied simultaneously. An overview of the specimen dimensions and test program is shown in Table 1.

4. Results and discussion

In this paper, the following definitions are used for interpreting the coefficient of determination R^2: very strong relationship $R^2 \geq 0.80$, strong relationship $R^2 \geq 0.60$, moderate relationship $R^2 \geq 0.40$, weak relationship $R^2 \geq 0.20$, and negligible relationship $R^2 < 0.20$.

4.1. Model validation

4.1.1. Wave propagation

For the assumption of a simply supported beam with a fully activated inertial field in Fig. 2, failure must occur after the shear waves c_s in Section 2.2 have propagated to the supports and back to the load application point. This condition ensures that the displacement measurements reflect the overall response rather than transient stages of the impact process, making them suitable for force estimation. As shown in Fig. 6, failure, indicated by black dots, in the tested specimens occurs after the completion of one to two shear wave cycles.

From the wavefront diagrams shown in Fig. 6, further observations can be made. The longitudinal waves c_l reach the supports first, followed by the shear waves c_s, while the bending waves c_{gb} are the last to arrive. For the 2.80 m specimens, the arrival times of the shear c_s and bending waves c_{gb} are close, whereas for the 4.80 m specimens a clear separation is evident. This suggests a non-linear increase in the difference between bending c_{gb} and shear wave c_s propagation velocities with increasing span length L. The non-linear relationship can be attributed to the influence of the natural frequency ω_n on the determination of the bending wave group velocity c_{gb}. Due to the material properties of timber, specifically the comparatively low elastic modulus E and low shear modulus G, it is essential to check the wavefront diagrams when performing dynamic tests to ensure that the underlying assumptions are valid regarding the steady-state response.

4.1.2. Spring stiffness

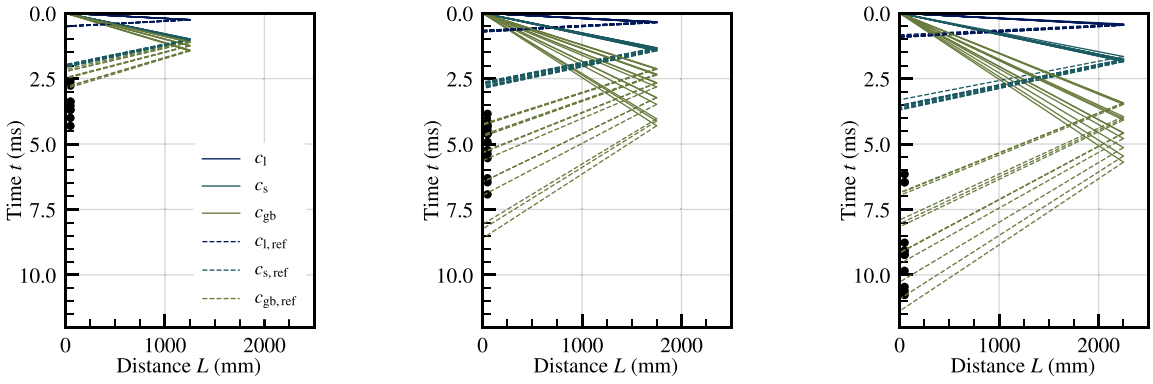
To verify which load model approximates the governing impact process best, the maximum bending stress with inertial forces and shear deformations $f^{\mathrm{in}}_{\mathrm{d,b,v}}$ is compared to models which neglect the contribution of these effects. As shown in Fig. 7(a), neglecting the inertial forces does not affect the coefficient of determination R^2 significantly. Contrary, as shown in Fig. 7(b), neglecting the shear effects leads to an insufficient model accuracy. As such, inertial effects can be neglected but the spring stiffness k should include shear deformations. The spring stiffness $k^{\mathrm{P}}_{\mathrm{b,v}}$ from Eq. (9) is therefore used for further calculations.

4.1.3. Energy balance

To verify the validity of the energy balance assumed in Eq. (3) and to ensure that no significant energy is lost through unquantified losses, the observed mean pendulum velocity $v_{\mathrm{pm,ArUco}}$ up to failure is compared to the mean velocity v_{pm} predicted from the energy balance. As shown in Fig. 8(a), some of the shortest specimens, exhibiting the highest velocities of approximately 9.5 m/s, show poor agreement with the predicted velocity v_{pm}. By limiting the discrepancy between predicted and measured velocities to 0.84 m/s at the observation point, equivalent to a 0.76 m/s difference at the pendulum's centre of mass L_{CM}, the coefficient of determination R^2 is improved. A discrepancy of 0.76 m/s at the centre of mass corresponds to an energy of approximately 1.00 kJ, which can be attributed to the variation of the dissipated energy E_{cl} of the release mechanisms. In relation to the release energy E_{r} the limit of 1.00 kJ represents a 5 to 10% accuracy.

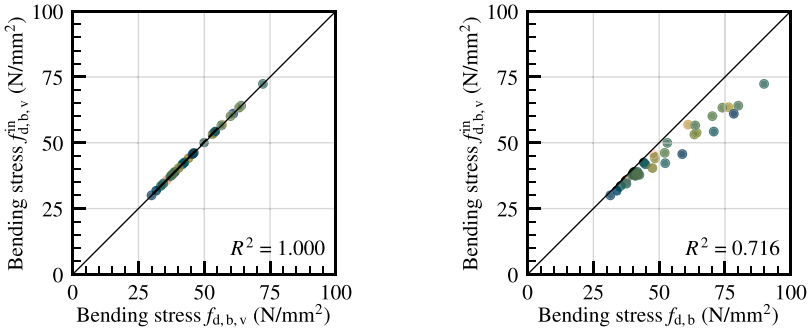
4.2. Impact and failure process

During the initial contact, the specimen and impactor experienced shock loading caused by the inertia of the stationary beam. At this stage, the impactor struck the beam with only local indentation visible. Following this, the impactor briefly separated from the beam before striking it a second time. This behaviour was rare in short specimens



(a) Specimen $L = 2.80$ m. (b) Specimen $L = 3.80$ m. (c) Specimen $L = 4.80$ m.

Fig. 6. Wavefront diagrams with time to failure t_f (black dots) for displacement measurement validity verification for impact velocities between 5.0 and 9.1 m/s. Solid lines indicate the arrival of longitudinal waves c_l, shear waves c_s, and bending waves c_{gb} at the supports, while dashed lines represent reflected waves returning to the centre of the specimen.



(a) Bending stress with shear and without inertial effects. (b) Bending stress without shear and inertial effects.

Fig. 7. Parity plot between different models of the maximum bending stress. The scatter is coloured according to the measured global modulus of elasticity E_{mg} with lighter colours indicating lower E_{mg} values and darker colours indicating higher values. (a) Comparison of maximum bending stress determined using spring stiffness including shear and inertial effects $k^{P,in}_{b,v}$ according to Eq. (8) and maximum bending stress determined using spring stiffness neglecting inertial effects and accounting for shear effects $k^{P}_{b,v}$ according to Eq. (9). (b) Comparison of maximum bending stress determined using spring stiffness including shear and inertial effects $k^{P,in}_{b,v}$ according to Eq. (8) and maximum bending stress determined using spring stiffness neglecting both inertial and shear effects k^{P}_{b} according to in Eq. (10).

but more pronounced in long specimens. For long specimens, transient stages were observed in which the free vibration of the beam following separation could be identified. As part of the kinetic energy had already been transferred during the initial contact, the beam and impactor remained in contact after the second impact in most cases.

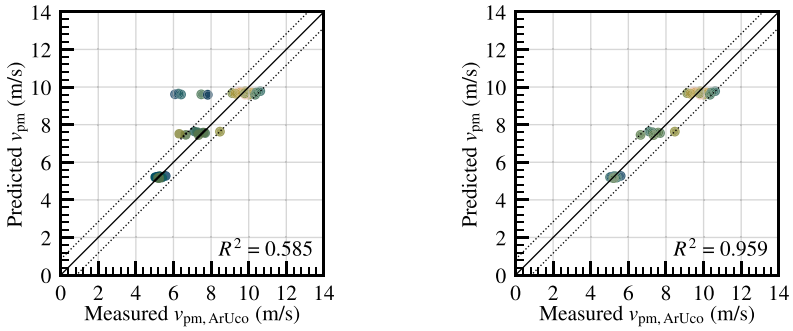
As shown in Fig. 9(a), after a certain duration, the first crack appeared. This this was not considered the point of failure. Failure was assumed only once a significant release within the lamellae was observed. This major release is shown in Fig. 9(b) and was characterised by a sudden distortion of the cross-section, indicating substantial stress redistribution. The full impact process is further described by Cao et al. [22].

Based on the work of Cao et al. [22], five failure mode classifications were adapted and expanded with a sixth mode. The sixth failure mode is finger-joint failure, as the tests by Cao et al. [22] were conducted on beams without finger-joints. The predominant failure mode was fibre bundle failure, occurring in 37.1% of the specimens. Mixed mode failure was observed in 22.9% of cases. Fibre failure occurred in 8.6% of specimens, considerably less frequent than knot failure (14.3%) and finger-joint failure (14.3%). Fibre failure and bond line failures were relatively rare. An overview of failure modes is shown in Table 2.

4.3. Dynamic strength increase factor

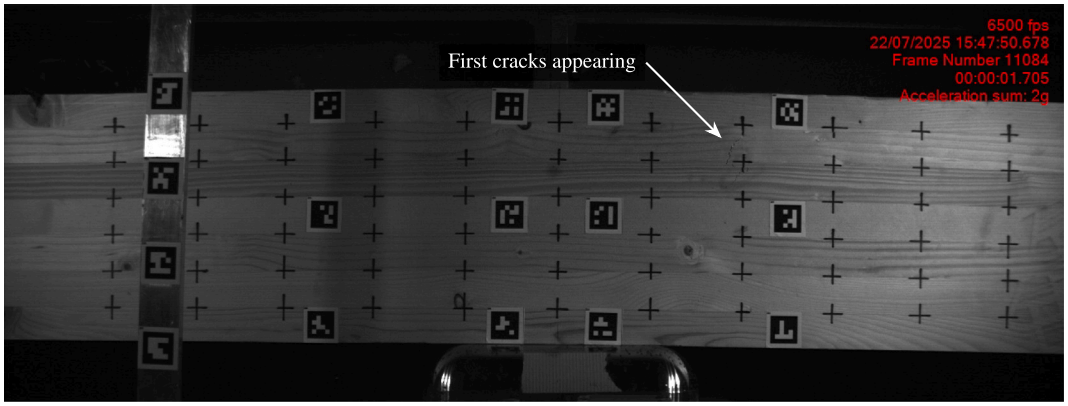
To derive a general constitutive relation for the rate-dependent behaviour of glued laminated timber beams, the datasets from existing literature and this study were first analysed separately. In a second step, all results were combined to assess the potential for an improved model.

Regarding the selection of fitting functions, a logarithmic, a quadratic polynomial, and a Cowper–Symonds strain rate regression function were initially considered. The logarithmic function produces a linear relationship on a logarithmic scale. According to Kuhn and Medlin [53], strain rates $\dot{\varepsilon} \leq 10^{-1}$ s^{-1} are considered quasi-static, where minimal to no rate-dependent effects are expected. Because of this property, the logarithmic function is unsuitable. It would imply

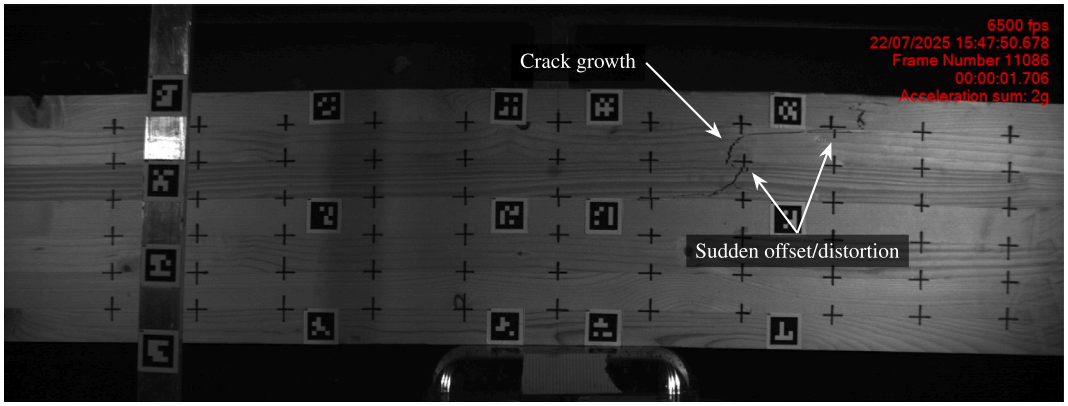


(a) Complete dataset. (b) Reduced dataset for 5–10% accuracy.

Fig. 8. Parity plot for energy balance verification. Measured mean pendulum velocity at the observation point plotted against the velocity predicted from the energy balance. Data points are coloured according to the measured global modulus of elasticity E_{mg} with lighter colours representing lower values and darker colours representing higher values. (a) Complete dataset with large deviations at high impact velocities, indicating intrinsic energy losses in the setup and the unsuitability of the specimens outside of the accepted energy variation. (b) Filtered dataset to reduce the absolute discrepancy between measured and predicted velocities at the observation point to a threshold of 0.84 m/s.



(a) Second impact with crack formation.

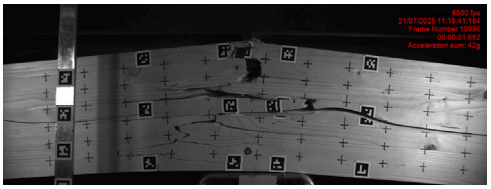
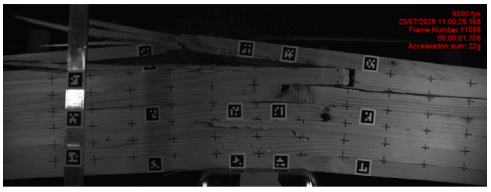
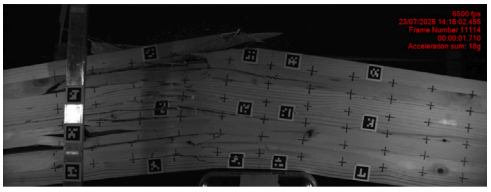
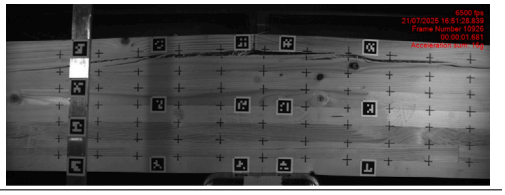


(b) High energy release, displacement tracking terminated at this point.

Fig. 9. Failure definition for displacement tracking. (a) Secondary contact of the impactor with the specimen, showing local indentation and the first visible crack development. This is not considered the failure point. Short specimens typically display a single contact, while longer specimens may exhibit brief separation followed by a second contact and transient free vibration. First crack formation sometimes occurred after the first impact or during the transient response. (b) Major energy release within the lamellae, indicated by sudden distortion of the cross-section and substantial stress redistribution. This is defined as the failure point for displacement tracking. Failure typically did not occur after the first impact or during the transient response for specimens subjected to multiple impacts.

strength increases in the quasi-static range. The quadratic polynomial and Cowper–Symonds power law yielded comparable results with a difference in the coefficient of determination R^2 of 0.01 and nearly identical curve shapes. Consequently, the Cowper–Symonds power law was selected. For consistency between four-point and three-point bending tests, the respective quasi-static reference tests in this paper were conducted using a three-point bending test configuration. This approach excludes any apparent bending resistance increase

Table 2
Failure modes for glued laminated timber subjected to impact loading adapted from Cao et al. [22].

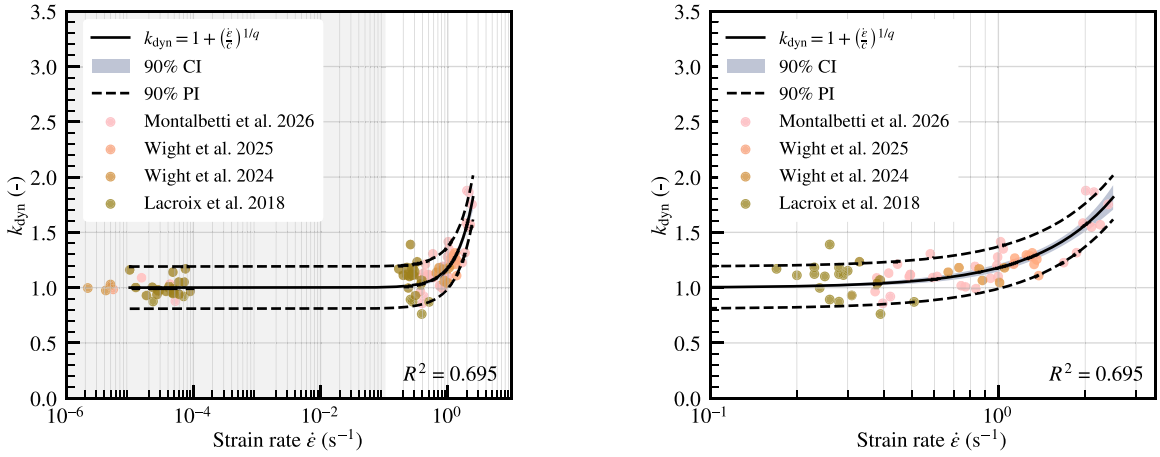
Failure mode (occurrence)	Picture
1. Fibre bundle failure (37.1 %) Tension failure occurs in bundled chunks of wood fibres. The failure is characterized by a rapid multi-lamella crack propagation.	
2. Mixed mode failure (22.9 %) A mix of all the failure modes. Knot failure, finger-joint, fibre bundle, or shear failure parallel to the grain often occurs first. These failures are often followed by wood fibre failures.	
3. Fibre failure (8.6 %) The wood fibres are pulled apart in small bundles or individually. The failure propagates gradually.	
4. Bond line failure (2.9 %) Cracks appear at or in the immediate vicinity of the bond lines. Longitudinal cracks propagate rapidly in a mode II failure, according to fracture mechanics.	
5. Knot failure (14.3 %) Cracks propagate rapidly from knot clusters or large grain deviations. Often occurs in combination with bond line failure or wood fibre failure.	
6. Finger-joint failure (14.3 %) Cracks propagate rapidly from finger-joints. Often occurs in combination with bond line failure or wood fibre failure.	

due statistical effects from the loading configuration, as described by Johnson [54].

As shown in Table 3, Cowper–Symonds regressions were developed based on a least square minimisation with the Python library SciPy [55], version 1.16.2. The regressions were developed and compared for the dataset of this study DS_1, the combined dataset of Lacroix and Doudak [19] DS_2 with Wight et al. [20,21] DS_3, the combined dataset of all the aforementioned studies $\sum DS_i$, and a filtered version of $\sum DS_i$ excluding outliers. When comparing the regressions of DS_1 and the combined dataset $DS_2\&DS_3$, DS_1 performed better for most metrics. The coefficient of determination $R^2 = 0.584$ indicates an almost strong relationship, which is higher than that of the combined dataset $DS_2\&DS_3$ with $R^2 = 0.332$, categorised as a weak relationship. Although the standard error of regression SER is higher, the F-test shows a better performance. The Durbin-Watson test DW indicates that the residuals of DS_1 show no positive autocorrelation, while $DS_2\&DS_3$ exhibit positive autocorrelation. The normality test of the residuals for DS_1 is inconclusive, as the performed tests yield conflicting results, whereas for $DS_2\&DS_3$ normality cannot be rejected. The combined dataset $\sum DS_i$ performs better than the individual datasets for almost all metrics. The coefficients of variation of the fitting parameters CV_i are significantly reduced, and the coefficient of determination R^2 increases. However, the normality of the residuals is rejected, as apparent in the QQ-plot shown in Fig. B.13(c). To address this, residuals with $Q_{\hat{e}} > 0.35$ were excluded, resulting in a final version of $\sum DS_i$ that performs best overall. With the exception of the standard error of regression SER and the Durbin-Watson test DW, all metrics improve, particularly the coefficient of determination R^2 and the normality tests of the residuals. Therefore, this final regression is proposed as a general constitutive relation for the rate-dependent behaviour of glued laminated timber with finger-joints. A depiction of the most important results of the regression analysis can be found in Appendix B.

The dynamic strength increase k_{dyn} results are shown in Fig. 10. Fig. 10(a) illustrates the full range of tested strain rates $\dot{\varepsilon}$, with the quasi-static regime defined by Kuhn and Medlin [53] highlighted in grey. To better illustrate the intermediate strain rate regime, Fig. 10(b) focuses on the dynamic range. The x-axis is shown on a logarithmic scale, as is common practice for rate-dependent constitutive relations, while the y-axis represents the dynamic strength increase k_{dyn} using Eq. (12).

In Fig. 11, the complete datasets, including outliers, from the four studies are compared to the calibrated Cowper–Symonds power law. In Fig. 11(a), it becomes apparent that the large spread of results around



(a) Full strain rate region from quasi-static to dynamic results.

(b) Intermediate strain rates [53].

Fig. 10. Dynamic strength increase factor k_{dyn}, where the dashed lines indicate the boundaries of the 90% prediction bound and the light blue area indicates the 90% confidence interval of the regression coefficients. (a) Full representation of the resulting dynamic strength increase factor k_{dyn} of the dataset $\sum DS_i$ w/o outliers from the quasi-static region indicated by the grey area to the intermediate strain rate region according to Kuhn and Medlin [53]. (b) Detailed representation of the dynamic strength increase factor k_{dyn} focused on the intermediate strain rate region of the dataset $\sum DS_i$ w/o outliers.

Table 3
Regression parameters. DS denotes the dataset, where DS_1 represents the data from this study, DS_2 the data from Lacroix and Doudak [19], and DS_3 the combined data from Wight et al. [20,21]. n is the number of samples, μ_i denotes the mean values, and CV_i the coefficients of variation of the fitting parameters. SER denotes the standard error of the regression, and %SER the normalised standard error of the regression. The autocorrelation of the residuals was evaluated using the Durbin-Watson test DW, while the normality of the residuals was assessed using the Jarque–Bera JB and Shapiro–Wilk W tests.

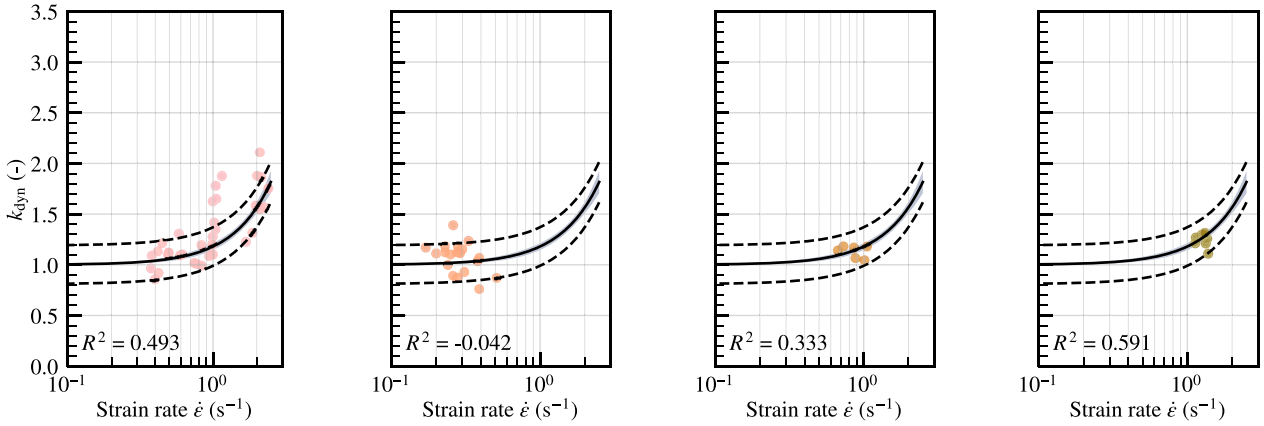
	DS_1	DS_2&DS_3	$\sum DS_i$	$\sum DS_i$ w/o outliers
n	38	57	95	89
μ_c	2.822	8.805	2.809	2.827
CV_c	0.123	0.797	0.084	0.060
μ_q	0.859	1.257	0.740	0.606
CV_q	0.193	0.351	0.126	0.104
R^2	0.584	0.332	0.591	0.695
CR^2	0.573	0.320	0.587	0.691
SER	0.0491	0.0169	0.0311	0.0677
%SER	0.0378	0.0158	0.0267	0.0602
F	50.57	27.30	79.62	125.05
d_L	1.37	1.50	1.62	1.61
d_U	1.59	1.65	1.71	1.70
DW	2.30	1.48	1.96	2.15
JB	3.848	4.778	30.688	0.204
	(0.146)	(0.092)	(0.000)	(0.903)
W	0.931	0.974	0.930	0.993
	(0.022)	(0.257)	(0.000)	(0.941)

a strain rate of $\dot{\varepsilon} = 10^0$ s^{-1} led to significant outliers, although most data still falls within the 90% prediction interval. The data shown in Fig. 11(b) includes a few outliers outside the 90% prediction interval that were not excluded. The coefficient of determination of $R^2 \approxeq 0$ means that the model does not perform better than the mean value of the data. This can be attributed to the large scatter. Overall, the general spread of the data remains within the bounds of the calibrated Cowper–Symonds power law. Fig. 11(c) and 11(d) demonstrate satisfactory agreement between the data and the developed regression, qualitatively and quantitatively. Three of the four addressed datasets can be categorised having a moderately weak to a strong relationship with the model.

4.4. Idealised softening ratio

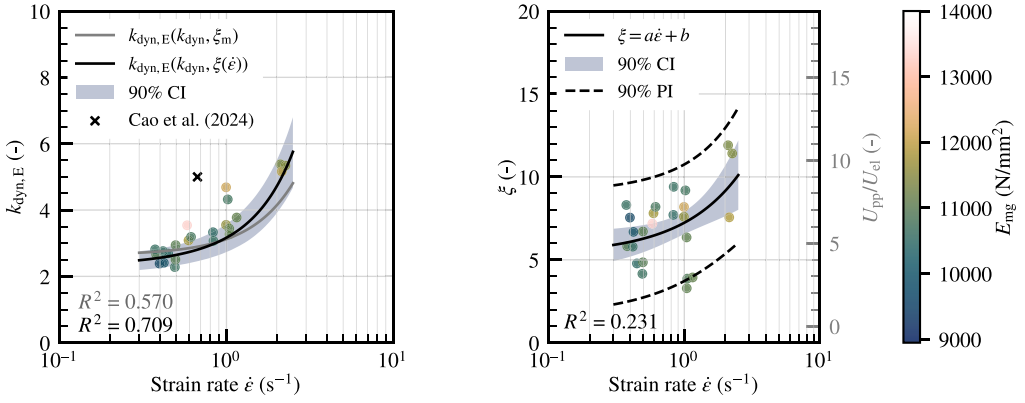
As shown in Fig. 12(a), the idealised impact force $P_{dyn,E}$ results in $k_{dyn,E}$ values that increase with increasing strain rate $\dot{\varepsilon}$. The values of the idealised impact force $P_{dyn,E}$ were calculated using the full integral in Eq. (16). In Fig. 12(b), the secondary axis in grey shows the ratio between the dissipated post-peak energy U_{pp} and the elastic strain energy U_{el}. The ratio U_{pp}/U_{el} is equal to $\xi - 1$. Previous tests conducted by Cao et al. [22] showed mean energy-equivalent dynamic increase values $k_{dyn,E}$ of 5.0 for spruce glued laminated timber without finger-joints at strain rates $\dot{\varepsilon}$ between 0.64 and 0.70 s^{-1}. As illustrated in Fig. 12(a), the results of the present study show energy-equivalent dynamic increase values $3.0 \lessapprox k_{dyn,E} \lessapprox 3.5$ within the same range of strain rates $\dot{\varepsilon}$. This highlights the influence of discontinuities, in this case finger-joints, on the energy dissipation potential of spruce glued laminated timber.

The energy-equivalent dynamic increase values $k_{dyn,E}$ can be expressed using the dynamic strength increase factor k_{dyn} and the softening ratio ξ through the relation in Eq. (19). If $k_{dyn,E}$ scaled perfectly with k_{dyn} and ξ, no correlation would be expected between the strain rate $\dot{\varepsilon}$ and the softening ratio ξ. However, this is not the case. A moderate positive correlation of $r = 0.48$ is observed. The perfect scaling assumption is illustrated by the grey curve in Fig. 12(a), where the mean softening ratio ξ is multiplied by the calibrated Cowper–Symonds power law in Fig. 11. The resulting model yielding a coefficient of determination $R^2 = 0.57$ may be regarded as satisfactory, but for high strain rates $\dot{\varepsilon}$, the model underestimates the energy-equivalent dynamic increase $k_{dyn,E}$ values. To address this limitation, a linear correction function was introduced for the softening ratio ξ. The corrected model, shown in Fig. 12(b), yields coefficients $a = 1.915$ and $b = 5.320$. A linear function was the only function achieving a coefficient of determination R^2 above 0.20, indicating a weak relationship. Logarithmic and polynomial fits resulted in $R^2 < 0.20$. By propagating the coefficient uncertainties of both the Cowper–Symonds power law in Fig. 10 and the linear regression in Fig. 12(b) through resampling, the black curve and its 90% confidence interval in Fig. 12(a) are obtained. The coefficient of



(a) This study. (b) Lacroix and Doudak [19]. (c) Wight et al. [21]. (d) Wight et al. [20].

Fig. 11. Comparison of regression results with various literature datasets. Dashed lines indicate the 90% prediction bounds and the light blue area shows the 90% confidence interval of the regression coefficients. (a) Regression performance for dataset DS_1 including outliers, with a coefficient of determination R^2 indicating moderate to strong goodness of fit. (b) Regression performance for dataset DS_2, showing large scatter and negligible improvement over the mean of the data points. (c) Dataset DS_3[21] exhibits weak to moderate goodness of fit. (d) Dataset DS_3[20] shows moderate to strong goodness of fit.



(a) Idealised impact force $P_{dyn,E}$. (b) Idealised softening ratio ξ.

Fig. 12. Energy-related quantities. The scatter is coloured according to the measured global modulus of elasticity E_{mg}. (a) Energy-equivalent dynamic increase $k_{dyn,E}$ as a function of strain rate $\dot{\varepsilon}$, calculated from the idealised impact force $P_{dyn,E}$. The grey curve shows the perfect scaling assumption obtained by multiplying the mean softening ratio ξ by the calibrated Cowper–Symonds power law. The black curve and shaded area indicate the corrected model with 90% confidence interval obtained via bootstrapping. The mean value of past experiments [22] is shown with a black cross. (b) Softening ratio ξ versus strain rate $\dot{\varepsilon}$, with the secondary grey axis showing the ratio of post-peak to elastic strain energy $U_{pp}/U_{el} = \xi - 1$. The regression coefficients for the linear correction of ξ are $a = 1.915$ and $b = 5.320$.

determination for the corrected extrapolation of the energy-equivalent dynamic increase factor $k_{dyn,E}$ increases to $R^2 = 0.709$, indicating a strong relationship.

5. Application example

Assume a rigid projectile travelling at a velocity $v_{p,0} = 10$ m/s with a mass $m_p = 1200$ kg impacting a member with dimensions $b \times h \times L = 300 \times 300 \times 4000$ mm, mean bending strength $f_m = 32.9$ N/mm^2 and modulus of elasticity $E = 11\,500$ N/mm^2 at the mid-span. Neglecting the intermediate kinetic energy transfer between the impactor and member, and assuming a triangular impulse shape, consistent with linear elastic material behaviour [4], results in an impact force P_d:

$$P_d = v_{p,0}\sqrt{m_p k} = 836 \text{ kN},$$

acting over a duration t_p:

$$t_p = 2\sqrt{\frac{m_p}{k}} = 28.7 \text{ ms},$$

with spring stiffness k:

$$k = k_b^P = \frac{48EI}{L^3} = 5\,822 \text{ kN/m}.$$

The strain rate $\dot{\varepsilon}$ follows from the assumed impulse shape:

$$\dot{P}_d = \frac{dP_d}{dt_p} = 2\frac{P_d}{t_p} \quad \rightarrow \quad \dot{\varepsilon} = \frac{\dot{M}_d}{EW_y} = \frac{\dot{P}_d}{EW_y}\frac{L}{4} = 1.125 \text{ s}^{-1},$$

giving a dynamic strength increase factor k_{dyn}:

$$k_{dyn} = 1 + \left(\frac{\dot{\varepsilon}}{c}\right)^{1/q} = 1 + \left(\frac{\dot{\varepsilon}}{2.827}\right)^{1/0.606} = 1.22.$$

The acting bending moment is multiplied by a dynamic amplification factor for a linear response $\lambda = 2.0$ [4], and compared with the resisting bending moment M_R:

$$M_R = W_y k_{dyn} f_{m,s} = 180 \text{ kNm} \ll \lambda\frac{P_d L}{4} = 1\,672 \text{ kNm},$$

therefore failure is expected. To assess whether the member can dissipate sufficient energy to arrest the projectile, the analysis is repeated using the energy-based strength increase factor:

$$k_{dyn,E} = \sqrt{k_{dyn}^2 \xi} = \sqrt{1.22^2 \cdot 7.47} = 3.33.$$

The acting bending moment is then compared with the resisting energy-based bending moment:

$$M_{R,E} = W_y k_{dyn,E} f_{m,s} = 493 \text{ kNm} \ll \lambda\frac{P_d L}{4} = 1\,672 \text{ kNm},$$

therefore, the projectile cannot be stopped by the member. The deceleration of the impactor due to the dissipated release energy is obtained from:

$$E_r = \frac{\xi P_{d,R}\delta_{el}}{2} = \frac{\xi P_{d,R}^2}{2k} = 20.9 \text{ kJ} \quad \therefore \quad \Delta v = -\sqrt{\frac{2E_r}{m}} = -5.90 \text{ m/s}.$$

To determine the final exit velocity of the impactor, the kinetic energy of the beam, determined using Eq. (24), must be subtracted additionally.

6. Conclusion

In this paper, 36 pendulum impact hammer tests were conducted on full-size spruce glued laminated timber beams with finger-joints. A wide range of strain rates was achieved by varying the beam length and the impact velocity simultaneously. A set of equations was developed to quantify the inertial and shear effects onto the spring stiffness during impact, allowing the ultimate resistance and accumulated strain energy to be determined from displacement measurements. The experimental results were used to quantify the dynamic strength increase factor and combined with existing literature to derive a rate-dependent constitutive relation for spruce glued laminated timber with finger-joints based on the Cowper–Symonds power law. Furthermore, the energy-related quantities, namely the energy-equivalent dynamic increase factor and an idealised softening ratio, were quantified. High-speed camera footage was used to assess the failures both qualitatively and quantitatively.

The results showed that inertial effects can be neglected for the governing masses and impact velocities. However, within the scope of this study, shear effects must be considered when determining the ultimate resistance from displacement tracking. The resulting dynamic strength increase factors are of similar magnitude to those reported in the existing literature for comparable specimens, confirming past findings and extending the available dataset. The mean dynamic strength increase factors vary between 1.00 and 1.70 depending on the strain rate, which is already reflected to some degree in several design codes. With regard to energy dissipation, the specimens absorbed between five and eight times the elastic energy in the post-peak phase. This deviates from the conventional assumption that timber behaves as an elastic-perfectly brittle material.

Limitations of this study include the absence of direct impact and reaction force measurements. The stress state was determined through a mechanical model, which represents only an approximation of the actual response. Incorporating load cells on the impactor and supports would further increase confidence in the results. In addition, to obtain a statistically meaningful regression, six outliers had to be removed from the current dataset. This corresponds to 16.6% of the tested specimens, which is a non-negligible proportion. For the energy-related quantities, the intrinsic but unquantified energy losses in the setup limited the accuracy to approximately 5 to 10%. Because it was not possible to separate the variation in dissipated energy associated with the release mechanism from the energy lost to vibration or elastic strain in the setup, further uncertainties were introduced into the energy-related results.

Additional tests at strain rates of approximately 1.0 and 2.0 s^{-1} could further improve the results. Most of the removed outliers occurred near a strain rate of 1.0 s^{-1}, and only three data points at around 2.0 s^{-1} were available for the energy-related calculations. Prior to implementing the developed regressions into design standards and guidelines, a risk- or reliability-based calibration should be conducted. The contribution of this study significantly improves the accuracy with which dynamic strength increase values should be applied. The calibrated constitutive relation relating the strain rate and dynamic strength increase factor may lead to more economical designs and is important for considerations in progressive collapse, vehicular impact, and similar loading scenarios. Moreover, the quantification of energy-related quantities enables performance-based design of members subjected to low-velocity impact, in which members may fully rupture while still ensuring that the energy carried by the projectile is fully dissipated.

CRediT authorship contribution statement

Gioele Montalbetti: Writing – review & editing, Writing – original draft, Validation, Methodology, Investigation, Formal analysis, Conceptualization. **Alex Sixie Cao:** Writing – review & editing, Validation, Supervision, Investigation, Conceptualization. **Andrea Frangi:** Writing – review & editing, Supervision, Project administration, Funding acquisition.

Declaration of generative AI and AI-assisted technologies in the manuscript preparation process

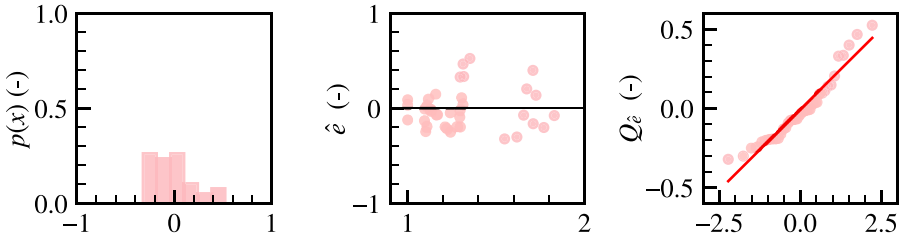
During the preparation of this work the author(s) used Google Gemini Enterprise and OpenAI ChatGPT in order to spell check and improve the readability of the manuscript. After using this tool/service, the author(s) reviewed and edited the content as needed and take(s) full responsibility for the content of the published article.

Declaration of competing interest

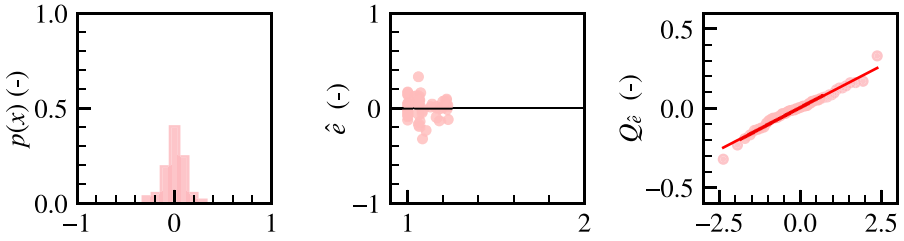
The authors certify that they have no affiliations with or involvement in any organisation or entity with any financial interest, or non-financial interest in the subject matter or materials in this manuscript.

Acknowledgements

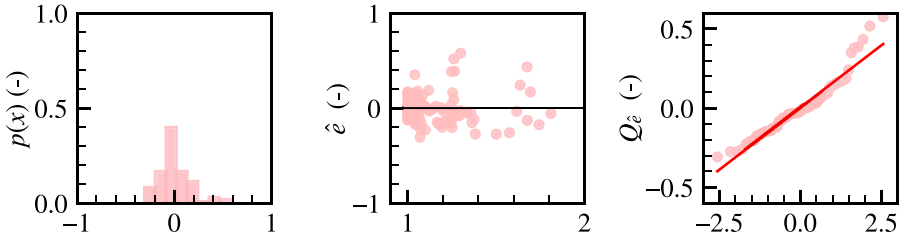
The authors gratefully acknowledge the financial support provided by *MainWood*, a Joint Initiative co-financed by the ETH Board, and funding from the *Chair of Structural Dynamics and Earthquake Engineering* at ETH Zurich. The authors would like to thank Annina Stadler, Jonas Ackermann, Maria Paula Felicita, Marie Keller, and the whole IBK Bauhalle team, who supported and contributed to the execution and safety of the experiments.



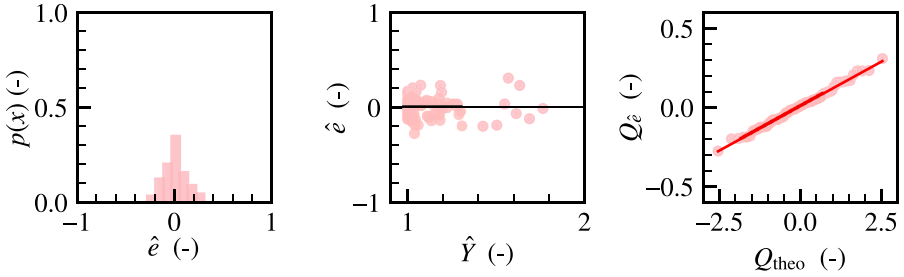
(a) Regression analysis DS_1



(b) Regression analysis DS_2&DS_3



(c) Regression analysis $\sum DS_i$



(d) Regression analysis $\sum DS_i$ w/o outliers

Fig. B.13. Residual analysis for regression development. The normalised residuals are denoted by $\hat{e}$, the model prediction is denoted by $\hat{Y}$, and the quantiles are denoted by Q_i.

Appendix A. Formula derivation

A.1. Inertial loading analytical solution

$$EI\frac{\mathrm{d}^4w}{\mathrm{d}x^4} - \kappa GA\frac{\mathrm{d}^2w}{\mathrm{d}x^2} = q(x)$$

$$q(x) = q_0\phi(x) = q_0\frac{x}{L^3}(3L^2 - 4x^2) = q_0\left(\frac{3x}{L} - \frac{4x^3}{L^3}\right)$$

$$V(x) = -\int q(x)\mathrm{d}x = -q_0\int \frac{3x}{L} - \frac{4x^3}{L^3}\mathrm{d}x = q_0\left(-\frac{3}{2}\frac{x^2}{L} + \frac{x^4}{L^3} + C_1\right)$$

$$M(x) = \int V(x)\mathrm{d}x = q_0\left(-\frac{1}{2}\frac{x^3}{L} + \frac{1}{5}\frac{x^5}{L^3} + C_1x + C_2\right)$$

Solve for rotation:

$$\varphi(x) = \frac{q_0}{EI}\int M(x)\mathrm{d}x = \frac{q_0}{EI}\left(-\frac{1}{8}\frac{x^4}{L} + \frac{1}{30}\frac{x^6}{L^3} + \frac{1}{2}C_1x^2 + C_2x + C_3\right)$$

$$\frac{\mathrm{d}w(x)}{\mathrm{d}x} = \gamma(x) - \varphi(x)$$

$$= \frac{V(x)}{\kappa GA} - \varphi(x)$$
$$= \frac{q_0}{\kappa GA}\left(-\frac{3}{2}\frac{x^2}{L} + \frac{x^4}{L^3} + C_1\right) + \frac{q_0}{EI}\left(\frac{1}{8}\frac{x^4}{L} - \frac{1}{30}\frac{x^6}{L^3} - \frac{1}{2}C_1x^2 - C_2x - C_3\right)$$

$$w(x) = \frac{q_0}{\kappa GA}\left(-\frac{1}{2}\frac{x^3}{L} + \frac{1}{5}\frac{x^5}{L^3} + C_1x\right) + \frac{q_0}{EI}\left(\frac{1}{40}\frac{x^5}{L} - \frac{1}{210}\frac{x^7}{L^3} - \frac{1}{6}C_1x^3 - \frac{1}{2}C_2x^2 - C_3x\right) + C_4$$

Boundary conditions $w(0) = 0$, $M(0) = 0$, $w'(L/2) = 0$, $V(L/2) = 0$. From the first two boundary conditions $w(0) = 0$, $M(0) = 0 \rightarrow C_4 = 0$ and $C_2 = 0$.

$$V(L/2) = -\frac{3}{2}\frac{L}{4} + \frac{L}{16} + C_1 = 0 \rightarrow C_1 = \frac{5L}{16}$$

$$\frac{\mathrm{d}w(L/2)}{\mathrm{d}x} = \frac{q_0}{\kappa GA}\left(-\frac{3}{2}\frac{L}{4} + \frac{L}{16} + \frac{5L}{16}\right) - \frac{q_0}{EI}\left(\frac{1}{8}\frac{L^3}{16} - \frac{1}{30}\frac{L^3}{64} - \frac{1}{2}\frac{5L^3}{64} - C_3\right) = -\frac{16L^3}{1920} - C_3 = 0 \rightarrow C_3 = -\frac{61L^3}{1920}$$

The solutions are therefore:

$$V(x) = q_0\left(-\frac{3}{2}\frac{x^2}{L} + \frac{x^4}{L^3} + \frac{5L}{16}\right)$$

$$M(x) = q_0\left(-\frac{1}{2}\frac{x^3}{L} + \frac{1}{5}\frac{x^5}{L^3} + \frac{5L}{16}x\right)$$

$$w(x) = \frac{q_0}{\kappa GA}\left(-\frac{1}{2}\frac{x^3}{L} + \frac{1}{5}\frac{x^5}{L^3} + \frac{5L}{16}x\right) + \frac{q_0}{EI}\left(\frac{1}{40}\frac{x^5}{L} - \frac{1}{210}\frac{x^7}{L^3} - \frac{5L}{96}x^3 + \frac{61L^3}{1920}x\right)$$

$$w'(x) = \frac{q_0}{\kappa GA}\left(-\frac{3}{2}\frac{x^2}{L} + \frac{x^4}{L^3} + \frac{5L}{16}\right) + \frac{q_0}{EI}\left(\frac{1}{8}\frac{x^4}{L} - \frac{1}{30}\frac{x^6}{L^3} - \frac{5L}{32}x^2 + \frac{61L^3}{1920}\right)$$

The closed solution for the deflection and bending moment at $x = L/2$:

$$w(L/2) = \frac{q_0L^2}{10\kappa GA} + \frac{17q_0L^4}{1680EI}$$

$$M(L/2) = \frac{q_0L^2}{10}$$

Appendix B. Regression analysis

See Fig. B.13.

Data availability

Data will be made available on request.

References

[1] Kunnath SK, Bao Y, El-Tawil S. Advances in computational simulation of gravity-induced disproportionate collapse of RC frame buildings. J Struct Eng 2018;144(2):03117003. http://dx.doi.org/10.1061/(ASCE)ST.1943-541X.0001938.

[2] Cao AS, Esser L, Frangi A. Modelling progressive collapse of timber buildings. Structures 2024;62:106279. http://dx.doi.org/10.1016/j.istruc.2024.106279.

[3] Montalbetti G, Cao A, Frangi A. Modelling vehicular impact for threat-dependent progressive collapse assessments. In: The 7th international conference on protective structures (ICPS7). Trans Tech Publications Ltd; 2025, http://dx.doi.org/10.4028/p-O4q45b, Pages: 24.

[4] Cao AS, Palma P, Frangi A. Dynamic amplification factors in instantaneously loaded structures. Eng Struct 2025;345:121464. http://dx.doi.org/10.1016/j.engstruct.2025.121464.

[5] Verleysen P, Peirs J, Van Slycken J, Faes K, Duchene L. Effect of strain rate on the forming behaviour of sheet metals. J Mater Process Technol 2011;211(8):1457–64. http://dx.doi.org/10.1016/j.jmatprotec.2011.03.018.

[6] Forni D, Chiaia B, Cadoni E. Strain rate behaviour in tension of s355 steel: Base for progressive collapse analysis. Eng Struct 2016;119:164–73. http://dx.doi.org/10.1016/j.engstruct.2016.04.013.

[7] Ghadiri MM, Agyapong J, Boakye-Yiadom S, Jian C. Rate dependence of high strength steels mechanical behavior: Characterization, modelling and impact applications. Int J Impact Eng 2025;206:105454. http://dx.doi.org/10.1016/j.ijimpeng.2025.105454.

[8] Tedesco JW, Powell JC, Ross CA, Hughes ML. A strain-rate-dependent concrete material model for ADINA. Comput Struct 1997;64(5):1053–67. http://dx.doi.org/10.1016/S0045-7949(97)00018-7.

[9] Abu-Lebdeh T, Hamoush S, Choi W, Nasra MA. High rate-dependent interaction diagrams for reinforced concrete columns. Am J Eng Appl Sci 2011;4(1):1–9. http://dx.doi.org/10.3844/ajeassp.2011.1.9.

[10] Cusatis G. Strain-rate effects on concrete behavior. Int J Impact Eng 2011;38(4):162–70. http://dx.doi.org/10.1016/j.ijimpeng.2010.10.030.

[11] Canadian Standards Association. CSA S850:23. Design and assessment of buildings subjected to blast loads. 2023.

[12] Ministry of Construction and Housing and Communal Services of the Russian Federation. SP 64.13330.2017. SNiP II-25-80 Wooden structures. Technical Report, Moscow, Russia: Ministry of Construction, Housing, and Communal Services of the Russian Federation; 2017.

[13] American Society of Civil Engineers. ASCE/SEI 59-11. blast protection of buildings. 2011.

[14] European Committee for Standardization. EN 1995-1-1:2004. eurocode 5: Design of timber structures, general - common rules and rules for building. 2004.

[15] Swiss society of engineers and architects (SIA). SIA 265:2021 timber structures. 2021.

[16] Wood LW. Relation of strength of wood to duration of load. 1960.

[17] Kohler J, Svensson S. Probabilistic representation of duration of load effects in timber structures. Eng Struct 2011;33(2):462–7. http://dx.doi.org/10.1016/j.engstruct.2010.11.002.

[18] Köhler J. Reliability of timber structures [Ph.D. thesis], ETH Zurich; 2006, http://dx.doi.org/10.3929/ETHZ-A-005164254.

[19] Lacroix DN, Doudak G. Determining the dynamic increase factor for glued-laminated timber beams. J Struct Eng 2018;144(9):04018160. http://dx.doi.org/10.1061/(ASCE)ST.1943-541X.0002146.

[20] Wight N, Viau C, Heffernan P. Cold temperature effects on the impact behaviour of glued-laminated timber beams. Int J Impact Eng 2025;195:105135. http://dx.doi.org/10.1016/j.ijimpeng.2024.105135.

[21] Wight N, Viau C, Heffernan P. Behaviour of glued-laminated timber beams under impact loading. Can J Civ Eng 2024;51(7):753–68. http://dx.doi.org/10.1139/cjce-2023-0298.

[22] Cao A, Houen M, Frangi A. Impact loading of glued laminated timber beams without finger-joints. Comput Struct 2024;296. http://dx.doi.org/10.1016/j.compstruc.2024.107278.

[23] Canadian Standards Association. CSA o177-23, qualification code for manufacturers of structural glued-laminated timber. 2023.

[24] Canadian Standards Association. CSA o122-16, structural glued-laminated timber. 2021.

[25] European Committee for Standardization. EN 14080:2013. timber structures - glued laminated timber and glued solid timber - requirements. 2013.

[26] Lacroix D, Doudak G. Investigation of dynamic increase factors in light-frame wood stud walls subjected to out-of-plane blast loading. J Struct Eng 2014;141. http://dx.doi.org/10.1061/(ASCE)ST.1943-541X.0001139.

[27] Cowper GR, Symonds PS. Strain-hardening and strain-rate effects in the impact loading of cantilever beams. Technical report TR-C11-28, Rhode Island, USA: Division of Applied Mathematics, Brown University; 1957, http://dx.doi.org/10.21236/AD0144762.

[28] Gupta MK, Singh NK, Gupta NK. Energy dissipation and notch sensitivity of mild steel at different strain rates and temperatures. Int J Impact Eng 2023;178:104610. http://dx.doi.org/10.1016/j.ijimpeng.2023.104610.

[29] Tanimura S, Tsuda T, Abe A, Hayashi H, Jones N. Comparison of rate-dependent constitutive models with experimental data. Int J Impact Eng 2014;69:104–13. http://dx.doi.org/10.1016/j.ijimpeng.2014.01.006.

[30] Feng Y, Xiao S, Yang B, Zhu T, Yang G, Zhu Z. Dynamic constitutive relation of 5083p-o aluminium alloy and its influence on energy-absorbing structure. Adv Mech Eng 2018;10(10):1687814018807334. http://dx.doi.org/10.1177/1687814018807334.

[31] Jočbalis G, Kačianauskas R, Borodinas S, Rojek J. Comparative numerical study of rate-dependent continuum-based plasticity models for high-velocity impacts of copper particles against a substrate. Int J Impact Eng 2023;172:104394. http://dx.doi.org/10.1016/j.ijimpeng.2022.104394.

[32] Somarathna HMCC, Raman SN, Mohotti D, Mutalib AA, Badri KH. Hyper-viscoelastic constitutive models for predicting the material behavior of polyurethane under varying strain rates and uniaxial tensile loading. Constr Build Mater 2020;236:117417. http://dx.doi.org/10.1016/j.conbuildmat.2019.117417.
[33] Zhou X, Ren W, Wang K, Zhu R, Xu L, Gao G. Tensile properties and constitutive modeling of kevlar29 fibers: From filaments to bundles. Int J Impact Eng 2025;196:105164. http://dx.doi.org/10.1016/j.ijimpeng.2024.105164.
[34] Kimberley J, Ramesh KT, Daphalapurkar NP. A scaling law for the dynamic strength of brittle solids. Acta Mater 2013;61(9):3509–21. http://dx.doi.org/10.1016/j.actamat.2013.02.045.
[35] Jeong H, Jeon B, Choi S, Jeon S. Fracturing behavior around a blasthole in a brittle material under blasting loading. Int J Impact Eng 2020;140:103562. http://dx.doi.org/10.1016/j.ijimpeng.2020.103562.
[36] Jameekornkul P, Panesar A. Dynamic behaviour of functionally graded lattice structures with short carbon fibre reinforcement. Int J Impact Eng 2026;208:105525. http://dx.doi.org/10.1016/j.ijimpeng.2025.105525.
[37] Baumann G, Czibula C, Hirn U, Feist F. The tensile behaviour of paper under high loading rates. Cellulose 2025;32(2):1201–19. http://dx.doi.org/10.1007/s10570-024-06266-0.
[38] Niemz P, Sonderegger W. Holzphysik: Eigenschaften, Prüfung und Kennwerte. 2021, http://dx.doi.org/10.3139/9783446470101.
[39] Goodwin J, Woods JE, Hoult NA. Assessing the structural behaviour of glued-laminated timber beams using distributed strain sensing. Constr Build Mater 2022;325:126844. http://dx.doi.org/10.1016/j.conbuildmat.2022.126844.
[40] Gomes Ferreira J, Cruz H, Silva R. Failure behaviour and repair of delaminated glulam beams. Constr Build Mater 2017;154:384–98. http://dx.doi.org/10.1016/j.conbuildmat.2017.07.200.
[41] Cao A, Frangi A. Dynamic strength increase of glued laminated timber beams subjected to impact loading. In: INTER proceedings meeting fifty-six 2023. Timber Scientific Publishing; 2023, p. 309–30. http://dx.doi.org/10.3929/ethz-b-000653637.
[42] Polocoşer T, Kasal B, Stöckel F. State-of-the-art: intermediate and high strain rate testing of solid wood. Wood Sci Technol 2017;51(6):1479–534. http://dx.doi.org/10.1007/s00226-017-0925-6.
[43] Giurgiutiu V. Structural health monitoring with piezoelectric wafer active sensors. second ed.. University of South Carolina, Columbia, SC, USA: Academic Press is an imprint of Elsevier; 2014, http://dx.doi.org/10.1016/C2013-0-00155-7.
[44] Biggs JM. Introduction to structural dynamics. McGraw-Hill, New York, NY; 1964.
[45] Blank L, Fink G, Jockwer R, Frangi A. Quasi-brittle fracture and size effect of glued laminated timber beams. Eur J Wood Wood Prod 2017;75. http://dx.doi.org/10.1007/s00107-017-1156-0.
[46] Martin JB, Symonds PS. Mode approximations for impulsively-loaded rigid-plastic structures. J Eng Mech Div 1966;92(5):43–66. http://dx.doi.org/10.1061/JMCEA3.0000787.
[47] Cao A, Houen MT, Lolli M, Frangi A. Pendulum impact hammer tests on glued laminated timber beams. Report, ETH Zurich; 2022, http://dx.doi.org/10.3929/ethz-b-000585619.
[48] Garrido-Jurado S, Muñoz-Salinas R, Madrid-Cuevas F, Marín-Jiménez M. Automatic generation and detection of highly reliable fiducial markers under occlusion. Pattern Recognit 2014;47:2280–92. http://dx.doi.org/10.1016/j.patcog.2014.01.005.
[49] Bradski G. The opencv library. Dr Dobb's J Softw Tools 2000.
[50] European Committee for Standardization. EN 408:2010. timber structures - structural timber and glued laminated timber - determination of some physical and mechanical properties. 2012.
[51] JCSS. Probabilistic model code: Part III - resistance models, timber. Joint Committee on Structural Safety; 2006.
[52] European Committee for Standardization. EN 384:2016. structural timber - determination of characteristic values of mechanical properties and density. 2018.
[53] Kuhn H, Medlin D. Introduction to high strain rate testing. In: Mechanical testing and evaluation. ASM International; 2000, p. 427–8. http://dx.doi.org/10.31399/asm.hb.v08.a0003293.
[54] Johnson AI. Strength, safety and economical dimensions of structures. In: Document / national Swedish building research 1971/7, Statens Institut för byggnadsforskning; 1971.
[55] Virtanen P, Gommers R, Oliphant TE, Haberland M, Reddy T, Cournapeau D, Burovski E, Peterson P, Weckesser W, Bright J, van der Walt SJ, Brett M, Wilson J, Millman KJ, Mayorov N, Nelson ARJ, Jones E, Kern R, Larson E, Carey CJ, Polat İ, Feng Y, Moore EW, VanderPlas J, Laxalde D, Perktold J, Cimrman R, Henriksen I, Quintero EA, Harris CR, Archibald AM, Ribeiro AH, Pedregosa F, van Mulbregt P, SciPy 10 Contributors. Scipy 1.0: Fundamental algorithms for scientific computing in python. Nature Methods 2020;17:261–72. http://dx.doi.org/10.1038/s41592-019-0686-2.